

# Nanomaterial-Based Soft Electronics for Healthcare Applications

Siddangouda Hosamani

Selection Grade Lecturer  
Electronics And Communication Engg Department  
Government Polytechnic Belgaum

Janappa R. Hugar

Selection Grade Lecturer  
Electronics And Communication Engg Department  
Government Polytechnic Bagalkote

## ABSTRACT

Due to their distinct benefits over traditional rigid electronics, soft digital equipment, particularly for smart healthcare, have been the subject of much study during the past 10 years. These benefits include conformal interactions on target tissues including the skin, heart, and brain in addition to a high degree of deformability that reduces unwelcome inflammatory reactions. For wearable and implantable implants, several strategies have been used to achieve mechanically soft but multi - functional high-performance electronics. These include designed gathering of high-quality nanomaterials, the fusion of unconventional production processes with existing tiny processing techniques, new device design features with deformable structures, and more and system-level integration of various soft electronics tailored to specific diseases.

We describe current developments in soft digital equipment for smart healthcare in this focus review. We go into more detail on innovative device design and integration strategies, assembly techniques for different nanomaterials, applications for textile-based and skin-attached wearable electronics, and their inclusion in fully-and/or minimally invasive medical devices. This research finishes with a succinct explanation of the future direction of healthcare applications utilizing soft bioelectronics based on nanomaterials.

**Keywords:** Nano Materials, Nano Technology, Electronics, healthcare, integrations

## I. INTRODUCTION

The electronics industry has concentrated on high speed and big capacity technologies like microprocessors and random-access memory since the 1920s, when the field effect transistor was invented. But the current development of customized and portable electronics has changed the focus of research from performance-oriented to human-friendly. [1] In light of this, flexible and stretchy electronics have been emphasized, whose mechanical characteristics are comparable to those of human tissues yet whose performances are on par with those of traditional electronics. The market for healthcare equipment has grown dramatically because of a rise in life expectancy, and there is a pressing need for novel medical devices to significantly improve current clinical practises. [3] Soft bioelectronics based on nanomaterials have recently received a lot of interest for usage in the healthcare industry due to their distinctive characteristics, such as medical multifunctionality, mechanical deformability, and exceptional performances [4]. Nanomaterials were crucial in attaining these special benefits. For instance, the meso-porous-silica nanoparticles' huge surface area

permits effective drug delivery, [1] the carbon nanotubes' distinctive deformability provides a flexible electrode,[4] and the graphene's particular chemical composition enables high mobility in soft electronics.

These soft-electronic-based biomedical devices have been created in wearable [5] and/or implantable [6] varieties. They can be divided more precisely into four distinct groups: Fabric-based wearable technology, skin-mounted electronics, completely implanted technology, and minimally invasive surgical equipment are the first four categories. The top-down processing and bottom-up synthesis of nanomaterials allows for multifunctionality and/or improved performance of soft electronic devices. Systems that are designed for certain organs and particular disease models are produced through special device designs and monolithic assembly of numerous devices.

### 1.1: COMBINING SOFT ELECTRONICS, DEFORMABLE DESIGNS, AND NANOMATERIAL ASSEMBLY

Soft bioelectronics has made use of a variety of nanomaterials, including 0D nanocrystals, 1D nanowires, and 2D nanomembranes, to enhance

device performance as well as achieve mechanical deformability and multifunctionality (Figure 1a). [9] Nanomaterials have unique physical, chemical, and electrical properties that are superior to those of their bulk counterparts. Examples include the quantum confinement effect of 0D quantum dots, [10] superparamagnetic magnetic nanocrystals, [11] unidirectional carrier transport of 1D nanowires, [7b] distinctive transparency and conductance of 2D graphene, [12] and mechanical flexibility and high mobility of 2D silicon naphthalene (Figure 1a; bottom-right). [13] As a result, monolithic nanomaterial integration in electronics and/or optoelectronics is crucial.

Their homogeneous and extensive assembly is necessary to produce the array of nanomaterial-based devices. The integration of nanomaterials into soft electronics has been accomplished via a variety of assembly processes, including spin casting, the Langmuir Blodgett (LB) method, mechanical molding, dry transfer printing, and lithography (Figure 1b). Making large-area, self-assembled monolayers of nanocrystals is simple with the LB approach. The creation of consistent and high aspect ratio micro-/nanostructures is made possible by externally applying heat, photons, and pressure to composites of polymers and nanomaterial fillers. Another effective method for placing nanomaterial assemblies on a 2D plane of micro- or nano-configurations is transfers printing. For the transfer of 2D semiconductors nanomembranes, atomic transfer printing using a structured stamp is frequently utilized.

## II. NUMERICAL EXPERIMENT

In the COMSOL Multiphysics program, which uses the finite element method to solve partial differential equations, we represent RRAM. For a certain device construction, the electrodynamic and heat transmission equations were calculated using the lump material properties.

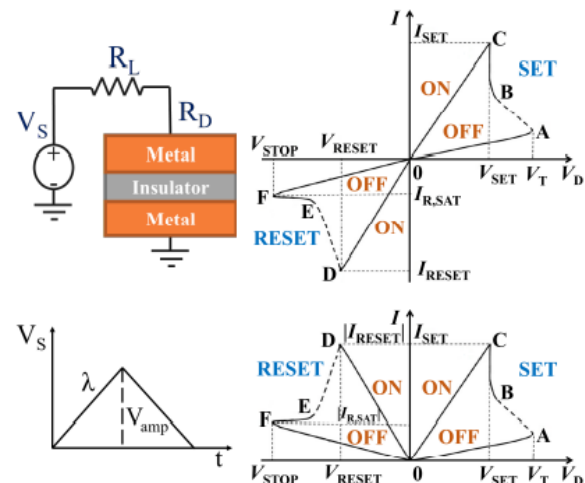


**Figure No. 1** - Top left: Circuitry diagram showing the series connection of a straightforward RRAM device ( $R_D$ ), a load resistor ( $R_L$ ), and an input voltage source ( $V_S$ ) in the circuit. Plot shows an input voltage pulse, where  $V_{amp}$  is the amplitude and is the voltage ramp-rate.

I-V properties of a typical RRAM are represented in the top right corner [4–7]. The RRAM device's voltage drop is denoted by  $V_D$ . The maximum current restricted by the  $V_{amp}$  is the SET current,  $I_{SET}$ . Traditional I-V depiction with an absolute valued current axis, bottom right. Extremely rapid nucleation processes are represented by the dashed domain.

The typical I-V is seen in Fig. 1 (right), and it has numerous domains that are connected to the device states and operations. The ON and OFF states that are unaltered by voltage ramping are represented by the domains C-0-D and A-0-F, respectively. A-B-C and D-E-F, on the other hand, show structural and electrical current fluctuations in response to source voltage ramping; they stand for the SET and RESET operations, respectively. Voltage snapback A–B followed by the vertical domain B–C for SET and voltage snap forward D–E followed by the horizontal domain E–F for RESET are their distinguishing characteristics.

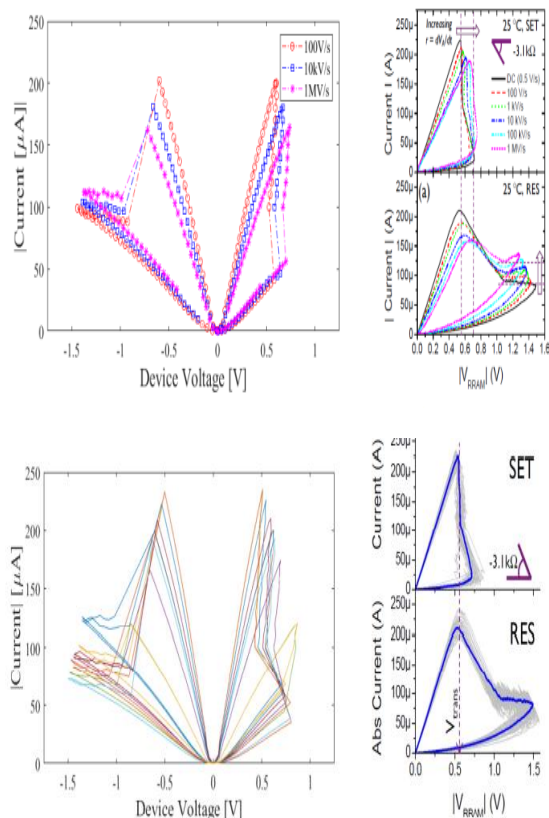


**Figure No. 2** - Simulated and experimental results are contrasted (c. 2012 IEEE). Reprinted from [4] with permission.) I-V for the same device the top figures show the applied voltage ramp-rate dependent I-V, while the bottom figures show the I-V change from cycle to cycle. In the right figures, 25°C is the ambient temperature, 3.1 k is the load resistor, VRRAM is the device voltage, and Vtrans is the SET voltage. Referring to the SET and RESET processes, respectively, is SET and RES. The rising SET voltage and faster-pulsing saturation current are shown in the top and bottom images, respectively, by the arrows. The I-V is displayed in the bottom right image for 50 cycles.

### III. OUTLINE

Here, we offer a condensed, "low-resolution," roadmap for further thought, some of which inevitably contain distracting elements. We begin by focusing on Fig. 2, which serves as the focal point of this study presentation. It shows how our model accurately replicates the reported RRAM properties, such as I-V changes with voltage ramp-rate and cycle-to-cycle. The paper is arranged as follows for further information.

#### 3.1: Physics

We outline the mechanics of RRAM operations. The field-induced nucleation of an

embryo with a needle-like shape is the first step in the development of conductive filament. As its length extends, it shunts the object and subsequently expands radially, at which point the resistance changes to the reciprocal of the current for domain BC. Due to the filament's limited capacitance, the charges build up. When the SET process is finished, the charged filament generates radial polarization, which freezes and persists intact in the ON state. The filament energy is reduced by the polarization-charge interaction.

Reversing bias polarity charges the filament in the other direction, rendering the polarization that was first formed energetically unfavorable. Reset occurs when the system's energy is raised by the polarization-charge interaction when the reversed bias reaches a high enough absolute value to break the filament and introduce an insulating gap into its structure. Reset occurs when the system's energy is raised by the polarization-charge interaction when the reversed bias reaches a high enough absolute value to break the filament and introduce an insulating gap into its structure.

#### 3.2: Modeling and Logic

We describe the numerical models in detail. We put into practice the gap nucleation mechanism for RESET processes and the field-induced nucleation mechanism for SET processes. The filament and gap development stages after nucleation are characterized as dissipative processes, where the temporal derivatives of the filament radius and gap width are proportional to the respective thermodynamic forces. When such forces disappear, or when the free energy is at its lowest, the equilibrium states are reached. In a similar vein, the filament parameters—thus, resistance and electric current—are generated by minimization of free energy under a given bias, which also predicts I-V shape.

As demonstrated in Fig. 2, we were able to replicate I-V with ramp-rate dependency and cycle-to-cycle volatility. We created a software that mimics how a gadget would actually operate. Control, six modules that represent the device states and switching operations, combined with switching circumstances, make up the programme. The software, which changes the modules when the switching requirements are met, is written in MATLAB, while the modules are built in COMSOL.

#### 3.3: Role of disorder

We introduce the configurational properties of non-crystalline materials, such the metal oxides employed in RRAM's insulator layer. In these materials, a certain percentage of atoms or groups of

atoms retain their mobility and have what are known as double well potentials, or two equilibrium states (DWP). The height of their activation barrier determines how quickly the two minima shift between each other. The ramp-rate dependency results from the applied bias's ability to activate DWP with relaxation periods less than the pulse duration. Because a device has such a small volume, it cannot contain enough DWPs to provide statistical self-averaging; instead, different implementations of nominally identical structures will have different ensembles of DWPs, which is what causes the variations in our numerical modelling from cycle to cycle.

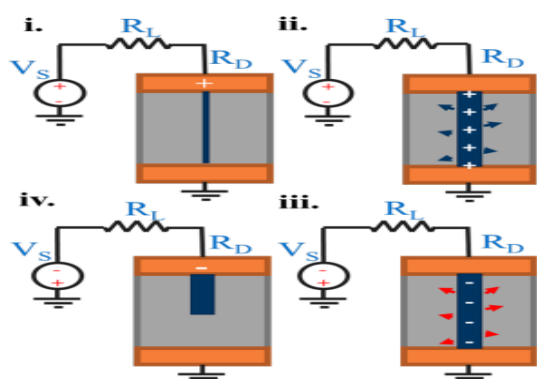


Figure No. 3 - Creating and destroying the filament in a typical multilayered metal-insulator-metal RRAM device. The polarization of the insulating host near the filament is represented by the arrows; the colors blue (ii) and red (iii) indicate energetically advantageous and unfavorable states, respectively. Please take note that the pictures are arranged in a cycle that corresponds to the SET and RESET switching cycle.

#### IV. METAL NPS-MEDIATED ROS PRODUCTION.

Nanomaterials have distinct physiological and chemical characteristics that set them apart from materials in either macroscopic (bulk) or atomic form because of the quantum size effect. There have been worries that these special characteristics might result in toxicity brought on by nanomaterials. It has been demonstrated that several nanomaterials, including metal NPs, carbon nanostructures, and semiconductor NPs, are harmful to living things. The production of ROS is a key factor in the toxicity caused by nanomaterials. The processes and key factors influencing the production of reactive oxygen species (ROS) by nanoparticles are covered in this special issue's review paper by Fu et al [58], titled "Mechanism of Nanotoxicityd Generation of Reactive Oxygen Species." We emphasize the

formation of ROS mediated by metal NPs in our presentation as an example for this review.

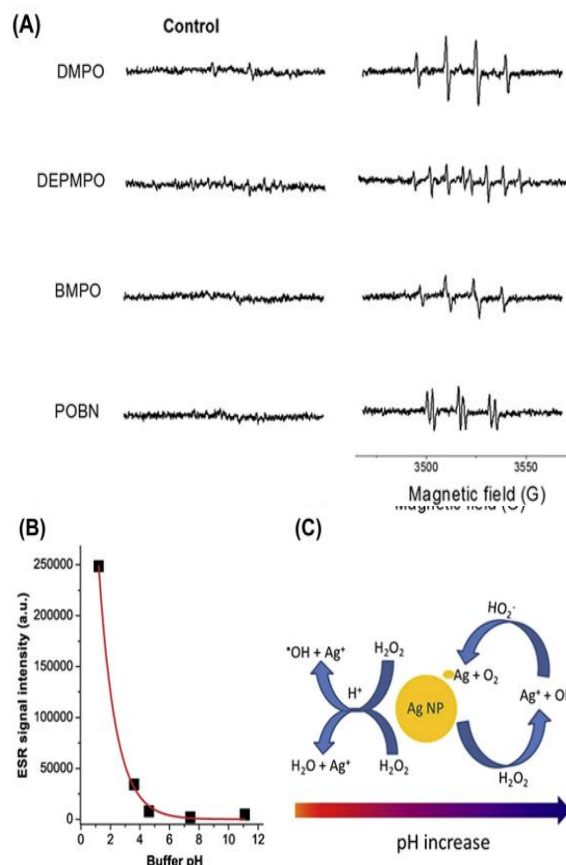


Figure No. 4 - Using various spin traps, (A) illustrates how hydroxyl radicals produced by Ag NPs in the presence of hydrogen peroxide at pH 3.6 (10mM acetate buffer). (B) Buffer pH and ESR signal strength. Ag NPs' (C) schematic portrayal of how pH controls the production of oxygen and hydroxyl radicals [4]. ESR [electron spin resonance; DMPO [5,5-dimethylpyrroline Noxide; NP [nanoparticle; POBN [ $\alpha$ -(4-pyridyl N-oxide)-N-tert-butyl nitron; BMPO [5-tertbutoxycarbonyl-5-methyl-1-pyrroline N-oxide; DEPMPO [5-diethoxyphosphoryl-5-methyl-1-pyrroline-N

There have been reports of a variety of metal NPs exhibiting intrinsic ROS generation or scavenging activities. Table 1 includes a summary of some typical findings, including NPs of the metals Ag, Au, Pt, Cu, Fe, Co, Ni Fe, and Co [4e6,60e84]. Under specific experimental circumstances, the capacity of Ag, Au, Cu, Fe, Ni, and Co NPs to cause the production of ROS has been shown. In different settings, Au NPs produce ROS, including OH, O<sub>2</sub><sup>•-</sup>, and O<sub>2</sub> [2, 5, 6, 8], whereas Ag NPs promote the generation of OH and O<sub>2</sub> [4, 6, 8]. Cu NPs have been shown to produce OH when hydrogen peroxide is present [15] and it

has been hypothesized that they will produce O<sub>2</sub> when DNA is present in phosphate-buffered saline [12].

Most of these investigations reported just the overall oxidative stress associated to ROS generation and utilized fluorescence probes rather than ESR to assess ROS. These findings show that ROS levels are greatly influenced by physiochemical parameters, such as the size, shape, composition, and surface coating of metal NPs. The two primary methods by which ROS are produced are the Fenton-like reaction and surface plasmon resonance amplification, both of which are covered in more depth in the following subsections.

#### 4.1 - ESR use for detecting ROS produced by nanomaterials

The bulk of macromolecules in biological systems are susceptible to oxidative damage from hydroxyl radicals because they are so highly reactive [87]. Because of its high reactivity [88] and brief half-life (approximately 1 millisecond), hydroxyl radicals are difficult to detect. Nevertheless, they quickly interact with diamagnetic nitron spin traps to produce stable free radicals (spin adducts), which may be recognized by the magnetic properties of the ESR spectrum. We have utilized ESR spin trapping to investigate how Ag and Au NPs interact with H<sub>2</sub>O<sub>2</sub> and produce hydroxyl radicals [4,5]. To characterize the production of hydroxyl radicals in the presence of H<sub>2</sub>O<sub>2</sub> and Ag NPs under acidic conditions, four spin traps—DMPO, BMPO, DEPMPO, and POBN—were used.

We saw ESR spectra that were distinctive of adducts created between each of the four spin traps and hydroxyl radicals in comparison to control conditions, showing that hydroxyl radicals are produced when the breakdown of hydrogen peroxide is aided by Ag NPs under acidic circumstances. Most significantly, as seen in Fig. 5, the formation of hydroxyl radical is influenced by the buffer pH as well as Ag NP size and concentration. Ag NPs' capacity to enable electron transfer in various chemical environments and H<sub>2</sub>O<sub>2</sub>'s pH-dependent redox activity have both been proposed as causes of the pH dependency and Ag NP-induced hydroxyl radical production (Fig. 5C). We also showed, using spin trapping ESR, that Au NPs may promote the production of hydroxyl radicals when hydrogen peroxide is present [5], with a pH dependency comparable to Ag NPs.

TiO<sub>2</sub> and ZnO are two examples of metal oxide NPs that are photo catalytically active and produce ROS when exposed to light. This photochemical activity has the potential to cause cytotoxicity under specific experimental

circumstances, especially those seen in in vitro experiments [9,89e91]. To test whether irradiated TiO<sub>2</sub> and ZnO NPs may generate hydroxyl radicals, we used DMPO or BMPO as a spin trap [89e91]. An ESR spectrum like that of the spin adduct DMPO/OH is seen when UV radiation is applied to TiO<sub>2</sub> in the presence of DMPO (Fig. 6A) [89]. We further investigated the production of hydroxyl radicals for various TiO<sub>2</sub> crystalline kinds using BMPO as a spin trap.

The outcomes demonstrated that rutile, anatase, and P25 can all create hydroxyl radicals when exposed to radiation, with P25 producing the greatest BMPO/OH signal (Fig. 6B) [9]. Like this, when exposed to UVA radiation, ZnO NPs can produce hydroxyl radicals in a dose-dependent way, which may cause human-derived keratinocytes to perish [91]. We used ESR spectroscopy in our joint research with other groups to show that iron oxide nanoparticles (Fe<sub>2</sub>O<sub>3</sub> and Fe<sub>3</sub>O<sub>4</sub> NPs, for example) may cause the generation of hydroxyl radicals in an acidic biological milieu through Fenton or Fenton-like reactions.

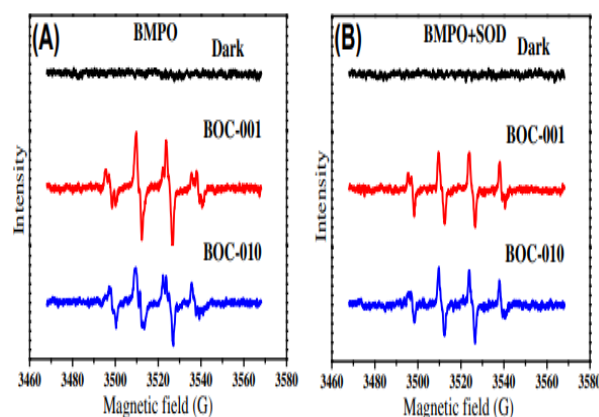


Figure No. 5 – ESR spectra of active oxygen radicals produced in BOC-001 and BOC-010 during photocatalysis under UV illumination (A) before and (B) after the addition of SOD [97]. BOC-001 [BiOCl with dominantly exposed face 001]; BOC-010 [BiOCl with dominantly exposed face 010]; ESR [electron spin resonance]; SOD [superoxide dismutase]; BMPO [5-tertbutoxycarbonyl-5-methyl-1-pyrroline N-oxide]

The most often utilized spin traps for spotting superoxide anions are DMPO and BMPO. Using DMPO as a spin trap, Harbour and Hair [95] have identified the superoxide produced by photoexcited CdS dispersions. Wang et al. [96] also employed the spin trap DMPO and the ESR method to analyze lit CdIn<sub>2</sub>S<sub>4</sub> microspheres. These researchers noticed the distinctive peaks of the DMPO/O<sub>2</sub> adducts in the irradiated methanol dispersion.

## V. VARIABILITY OF RRAM PARAMETERS: DISORDER-RELATED EFFECTS

One of the most typical characteristics of filamentary RRAM formations is the material's non-crystallinity. Some atoms or groups of atoms in a nanocrystalline substance nevertheless have some mobility and can switch between two equilibrium locations. DWP is used to characterize this trait [9, 30-32]. (Appendix C provides a brief description of a three-atomic DWP structural model to aid with intuitive understanding.) The relevance of DWP in this context is that they will apply this or another force to the system based on their local setups. A DWP-induced deformation that moves the mobility edges and has an exponentially significant impact on resistivity is a clear illustration of how this happens.

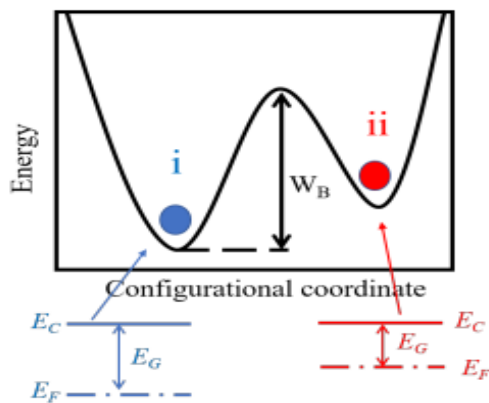


Figure No. 6: Diagram showing a twin well potential with two configurations divided by a WB barrier height. Each design has a unique deformation potential and hence a unique band gap.

The energy diagram of DWP is shown in Figure 6, where the presence of an energy barrier with unpredictable height  $W_B$  is significant. The relevant downtime is indicated by,

$$T = T_0 \exp \frac{W_t}{K_t} \text{ where } W_t = kT \ln \left( \frac{T}{T_0} \right)$$

The latter connection demonstrates that only DWP with barriers below  $W_B$  will participate in the process by altering their configurations at a certain relaxation period.

$$g(W_b) \approx \frac{1}{\Delta W_b}, \Delta W_b = W_{b,max} - W_{b,min}$$

Given by is the relevant relaxation-time distribution,

$$\rho(T) = g(W_t) \left| \frac{dW_t}{dt} \right| - \frac{K_t}{tW_t} \text{ where } t_{min} < t < t_{max}$$

where min and max represent, respectively, the minimum and maximum barrier heights. The two subsections that follow cover the main points of this DWP application.

### 5.1: The average rate dependent effect

The voltage pulse length, which is the reciprocal of the ramp-rate, is here designated as. The entire influence becomes proportional to their fractional concentration since only DWP with relaxation periods less than may alter their states.

$$f(T) = \frac{Kt}{\Delta W_b} \ln \left( \frac{T}{T_{min}} \right) \text{ for } t_{min} < t < t_{max}$$

denotes the influence of pulse rate on the observed RRAM characteristics, and was calculated by integrating Eq. 8 from min to max.

The variations in chemical potentials seen in Fig. 4 determine how the free energy varies because of phase transformations. We consider how these free energy differentials will alter because of the DWP transitions, which leads to,

$$\delta\mu_1 = \overline{\delta\mu_1} + \beta_1 kT \left( \frac{1}{\Delta W_{Buc}} - \frac{1}{\Delta W_{Bi}} \right) \ln \frac{\tau}{\tau_{min}}, (1)$$

$$\delta\mu_2 = \overline{\delta\mu_2} + \beta_2 kT \left( \frac{1}{\Delta W_{Buc}} - \frac{1}{\Delta W_{Bmc}} \right) \ln \frac{\tau}{\tau_{min}} (2)$$

Where  $\delta\mu_1$  and  $\delta\mu_2$  represent DWP independent contributions, and 1 and 2 are the proportionality coefficients that must be changed together with 1 and 2 during the modelling process.

## VI. CONCLUSION

In this focus review, we have covered current developments in soft bioelectronics for wearable and implantable biomedical applications that make use of assembled nanomaterials, strain relief designs, and diverse integrated electronics. The importance of soft electronics in medicine keeps growing because of various benefits including conformal connections, high deformability, and a biocompatible surface. Soft electronics have found extensive use in a variety of sectors, including 1) textile-based electronics, 2) skin-originated devices, 3) implanted instruments, and 4) minimally invasive surgical equipment.

Unconventional functionalities in therapeutic processes are made possible by the integration of different nanomaterials. The efficiency and efficacy of medical sensing, diagnosis, and therapy are increased by multifunctional systems based on integrated soft electronics, whose design is tuned for a specific disease model. Despite significant technological advancements, several problems persist and need more research. Applying silver nanowires and semiconducting nanocrystals (such as CdS, CdSe, and PbSe) to biomedical devices will require resolving toxicity difficulties. Gold nanowires and heavy metal-free nanocrystals like CISE and InP are suitable substitutes. For the mass manufacturing and commercialization of nanomaterials, larger-scale

advances in uniform and repeatable synthesis are also necessary.

It is necessary to enhance the tissue-device interaction. It is crucial to continue researching the long-term biocompatibility of nanomaterials, especially in implanted devices. Designs that allow for strong interfacial adhesion and strain relief can improve measurement quality, permit long-term attachment, and reduce immunological reactions. To commercialize soft bioelectronics, more procedures such as big animal trials, human applications, and assessments on small animals are required. Innovative clinical methods and protocols for the management of various diseases can be implemented by medical systems that include flexible sensors, memory devices, wireless modules, energy-harvesting devices, and therapeutic actuators. Another major objective of the device development is to provide implanted electronics with a continuous, reliable, and long-lasting power source. The development of soft bioelectronics would open the door to smart surgery and universal healthcare.

## REFERENCES

- [1]. Fantini, D. J. Wouters, R. Degraeve, L. Goux, L. Pantisano, G. Kar, Y.-Y. Chen, B. Govoreanu, J. A. Kittl, L. Altimime, and M. Jurczak, Intrinsic Switching Behavior in HfO<sub>2</sub> RRAM by Fast Electrical Measurements on Novel 2R Test Structures, 2012 4th IEEE International Memory Workshop, Milan, pp. 1-4 (2012)
- [2]. D. J. Wouters, L. Zhang, A. Fantini, R. Degraeve, L. Goux, Y. Y. Chen, B. Govoreanu, G. S. Kar, G. V. Groeseneken, and M. Jurczak, Analysis of Complementary RRAM Switching, *IEEE El. Dev. Letts.*, 33, pp. 1186-1188 (2012)
- [3]. I. V. Karpov, M. Mitra, D. Kau, G. Spadini, Y. A. Kryukov, and V. G. Karpov, Fundamental drift of parameters in chalcogenide phase change memory, *J. Appl. Phys.*, 102, 124503 (2007).
- [4]. G. Bersuker, J. Yuma, L. Vandelli, A. Padovani, L. Larcher, V. Iglesias, M. Porti, M. Nafra, K. McKenna, A. Shluger, P. Kirsch, and R. Jammy, Grain boundary driven leakage path formation in HfO<sub>2</sub> dielectrics, *Solid State Electronics*, 6566, 146150 (2011). OFF- Trap assisted tunneling.
- [5]. S. Y. Yang, E. D. O'Ceirbhail, G. C. Sisk, K. M. Park, W. K. Cho, M. Villiger, B. E. Bouma, B. Pomahac, J. M. Karp, *Nat. Commun.* 2013, 4, 1702.
- [6]. K.-I. Jang, S. Y. Han, S. Xu, K. E. Mathewson, Y. Zhang, J.-W. Jeong, G.-T. Kim, R. C. Webb, J. W. Lee, T. J. Dawidczyk, R. H. Kim, Y. M. Song, W.-H. Yeo, S. Kim, H. Cheng, S. I. Rhee, J. Chung, B. Kim, H. U. Chung, D. J. Lee, Y. Yang, M. Cho, J. G. Gaspar, R. Carbonari, M. Fabiani, G. Gratton, Y. Huang, J. A. Rogers, *Nat. Commun.* 2014, 5, 4779.
- [7]. L. Y. Chen, B. C.-K. Tee, A. L. Chortos, G. Schwartz, V. Tse, D. J. Lipomi, H.-S. P. Wong, M. V. McConnell, Z. Bao, *Nat. Commun.* 2014, 5, 5028.
- [8]. S. Xu, Y. Zhang, J. Cho, J. Lee, X. Huang, L. Jia, J. A. Fan, Y. Su, J. Su, H. Zhang, H. Cheng, B. Lu, C. Yu, C. Chuang, T.-i. Kim, T. Song, K. Shigeta, S. Kang, C. Dagdeviren, Petrov, P. V. Braun, Y. Huang, U. Paik, J. A. Rogers, *Nat. Commun.* 2013, 4, 1543.
- [9]. C. Pang, J. H. Koo, A. Nguyen, J. M. Caves, M.-G. Kim, A. Chortos, K. Kim, P. J. Wang, J. B.-H Tok, Z. Bao, *Adv. Mater.* 2015, 27, 634-640.
- [10]. D. Niraula and V. Karpov, Numerical modeling of resistive switching in RRAM device, Proceedings of the 2011 COMSOL Conference in Boston (2011)
- [11]. C. Walczyk, D. Walczyk, T. Schroeder, T. Bertaud, M. Sowinska, M. Lukosius, M. Frascchke, D. Wolansky, B. Tillack, E. Miranda, and C. Wenger, Impact of Temperature on the Resistive Switching Behavior of Embedded HfO<sub>2</sub>-Based RRAM Devices, *IEEE Trans. On El. Dev.*, 58, 3124 (2011). OFF-Poole-Frenkel,
- [12]. E. I. Levin, I. M. Ruzin, and B. I. Shklovskii, Transverse hopping conductivity of amorphous films in strong electric fields, *Sov. Phys. Semicond.*, 22(4), 407 (1988).
- [13]. J. D. Eshleby, The Continuum Theory of Lattice Defects, Editors Frederick Seitz, David Turnbull, *Solid State Physics*, Academic Press, 3, 79-144 (1956)
- [14]. u. M. Galperin, V. G. Karpov, and V. I. Kozub, Localised states in glasses, *Advances in Physics*, 38, 669 (1989).
- [15]. Sh. Kogan, *Electronic noise and fluctuations in solids*, Cambridge University Press, 1996.